Junction Photovoltge (JPV) Techniques for Ultra-Shallow Junction Characterization

V.N. Faifer[a], M.I. Current[a], D.K. Schroder[b], T. Clarysse[c], W. Vandervorst[c,d]

[a]Frontier Semiconductor, 199 River Oaks Parkway, San Jose CA,
[b]Department of Electrical Engineering, Arizona State University, Tempe, AZ 85287-5706
[c]IMEC, Kapeldreef 75, B-3001 Leuven, Belgium
[d]K.U.Leuven, Electrical Engineering Dept., INSYS, Kasteelpark Arenberg 10, B-3001 Leuven, Belgium

A non-contact method for measurement of sheet resistance and leakage current (RsL) for ultra-shallow junction (USJ) characterization is described based on analysis of frequency-dependent junction photovoltages from p-n junctions. Theoretical, device-simulated and measured photovoltages, sheet resistance as well as RsL and reverse-biased diode currents are compared. The linkage between RsL recombination currents and end-of-range implant damage in USJ/halo profiles and deletion layers is described. The addition of a Halo profile to a USJ results in increased sheet resistance and leakage current due to changes in the junction depth and depletion layer conditions. Measured recombination leakage currents for implanted and CVD-grown USJs are compared with calculation and show good agreement.

Introduction

Advanced USJ technology, using low energy implants and millisecond anneals, has encouraged the development of non-contact junction monitoring metrology. One-dimensional, frequency dependent, non-steady-state surface photo-voltage (SPV) theory for oxidized silicon wafers was developed the mid-1970s [1]. One-dimensional, frequency-dependent SPV theory was developed and applied to characterization of silicon epitaxial layer lifetime [2]. In 1960, Lucovsky [3] developed two-dimensional junction photovoltage (JPV) theory for abrupt box like doping profiles pn junctions and derived steady state analytical equations describing JPV distribution inside and outside of illumination area. A two-dimensional, non-steady-state approach was used to explain measured lateral spreading of surface photo-voltage inside and outside an illuminated area in oxidized Si wafers with strong inversion [4].

Verkuil developed the first non-contact method and apparatus for the measurement of sheet resistance using junction photovoltages from two metal rings placed outside an illumination area in 1995 [5]. The approximate equation that he used for the calculation of the ratio of the relevant photovoltages was valid only for infinitely thin rings. This technique can be used only if the pn junction capacitance is known through measurements by another technique. These disadvantages limit the use of Verkuil methods for accurate monitoring of USJs formed in halo and well profiles.

A rigorous two-dimensional, frequency-dependent non-steady-state junction photovoltage method was developed and implemented for measuring sheet resistance and leakage currents (RsL method) in p-n junctions with complex doping profiles [6,7]. Analytical equations for junction photovoltages were derived using a one-dimensional Poisson equation and integrating the three-dimensional continuity equation over the

vertical spatial coordinate perpendicular to the wafer surface [6]. Good correlation of this contactless technique with standard four-point probe (4PP) measurements was demonstrated for deep and low-leakage current p-n junctions [7]. In the case of USJs formed in heavily-doped regions, *e.g.*, with halos or wells, RsL and 4PP measurements of sheet resistance often give significantly different values due to substrate currents arising from contract probe penetration damage and high p-n junction leakage current. Recently, various RsL techniques were analyzed with detailed analytical modeling and numerical simulation [8]. Errors in measuring sheet resistance with standard 4PPs and good results with non-contact RsL techniques were demonstrated for CVD USJs formed on the top of moderately-doped ($7x10^{17}$ cm^{-3}) epi layers with junction thicknesses ranging down to less than 10 nm formed in moderately-doped ($7x10^{17}$ cm^{-3}) epi layers 20 μm thick [9]. Advantages of the RsL technique for monitoring of USJs formed with low-energy implants with millisecond anneals and thin low-temperature CVD-growth were demonstrated in [10-13].

Millisecond annealing methods, based on scanned laser beams or pulses of light from flash-lamp arrays, are designed to minimize dopant diffusion during annealing [10]. Although ms-timescale anneals have demonstrated very high levels of dopant activation, combined with minimal diffusion, recent studies have suggested that they do not completely remove all the damage introduced by conventional implant schemes. CVD approaches for USJ formation can lead to high interface state densities and also face many difficult challenges in process integration [14]. Residual damage after millisecond anneals increases the carrier recombination rate and the junction leakage current, especially for USJ formed in combination with highly-doped halo profiles [15]. For this reason, the monitoring of leakage current and sheet resistance of USJs formed in halo or highly-doped epilayers profiles is important, especially for advanced ULSI technology. At the same time, high leakage current density of $>10^{-4}$ A/cm^2, due to band-to-band and trap-assisted tunneling [15,16,17,18] makes sheet resistance measurements of USJ formed in highly-doped profiles with $N_D>10^{18}$ cm^{-3} difficult even using advanced non-penetrating four-point probes. Leakage current measurements require time consuming and expensive fabrication of special devices. For this reason non-contact monitoring of sheet resistance and leakage current has become very important for fast process control of advanced ULSI technology. In [10-13] it is shown that formation of shallow junctions in halo profiles strongly alters the sheet resistance and leakage current characteristic with respect to USJs formed in lightly doped substrate.

The present paper outlines the basics of RsL techniques for measurement of sheet resistance and leakage current and the comparison with reverse-biased diode leakage.

Photovoltage Measurements

The basis of the RsL measurement is to use photo-excitation of carriers in a p-n junction and wafer substrate and to monitor, in a spatially resolved manner, the JPV signals inside and outside the illumination area, when absorption of modulated light flux, $\Phi(t) = \Phi_0(1-\cos(2\pi ft))$, creates electron–hole pairs in the semiconductor material. Two electrodes, a circular transparent electrode (1) with diameter $2r_0$ at the center of the probe and second round arc conducting electrode (2) subtending an angle β and coaxial with the first electrode a small distance away, are used to measure JPV voltages V_1 and V_2 (Fig. 1) [6].

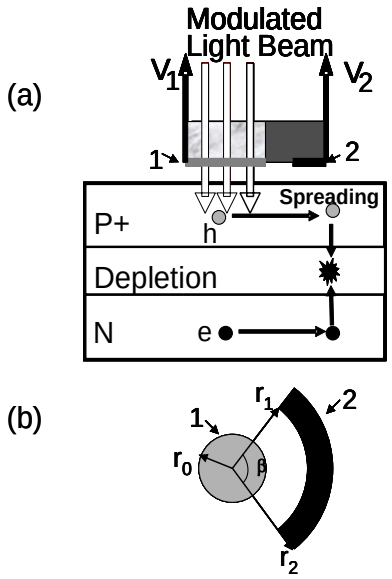

Figure 1.(a) Photo-excitation and carrier drift with a modulated light source and two capacitor electrodes for monitoring the induced junction photovoltage in a spatially resolved manner; (b) electrode configuration.

The JPV voltages V_1 and V_2 under low-level excitation are given by

$$V_1 = \frac{q\eta(1-R)\Phi_0 R_S}{k^2}\left[1 - 2I_1(kr_0)K_1(kr_0)\right] \tag{1}$$

$$V_2 = q\eta\frac{(1-R)\Phi_0\beta R_S}{\pi k^2 r_0} I_1(kr_0)\left[r_1 K_1(kr_1) - r_2 K_1(kr_2)\right] \tag{2}$$

$$k = \sqrt{R_S G_{p-n} + i2\pi f R_S C_{p-n}} \tag{3}$$

where I_0, I_1 , K_0 and K_1 are modified Bessel functions, Φ_0 the incident photon flux density modulated at frequency f, R the reflectivity, η the quantum efficiency, R_S, $G_{p\text{-}n}$, $C_{p\text{-}n}$ the p-n junction sheet resistance, capacitance and conductance [7,8]. Under illumination, the p-n junction is forward biased (V>0) and the p-n junction voltage at low excitation is V<< V_T =kT/q, where q is the electron charge, k Boltzmann's constant, and T the wafer temperature *(K)*. The junction conductance, $G_{p\text{-}n}$, and leakage current density measured using RsL method, J_{RsL}, are defined as

$$G_{p-n} = \left.\frac{dJ}{dV}\right|_{V\to+0} = J_{RsL}/V_T \tag{4}$$

where *J(V)* is the p-n junction current density.

For an ideal diode,

$$J(V) = J_0[\exp(V/V_T) - 1] \tag{5}$$

and the he RsL leakage current density, J_{RsL} , simply equals the prefactor J_0.

V_1 and V_2 versus light modulation frequency for high and low leakage current densities are shown in Fig. 2, demonstrating higher sensitivity of the JPV voltages to leakage current at low frequencies, when the contribution of $G_{p\text{-}n}$*R_s in Eq. (3) becomes important.

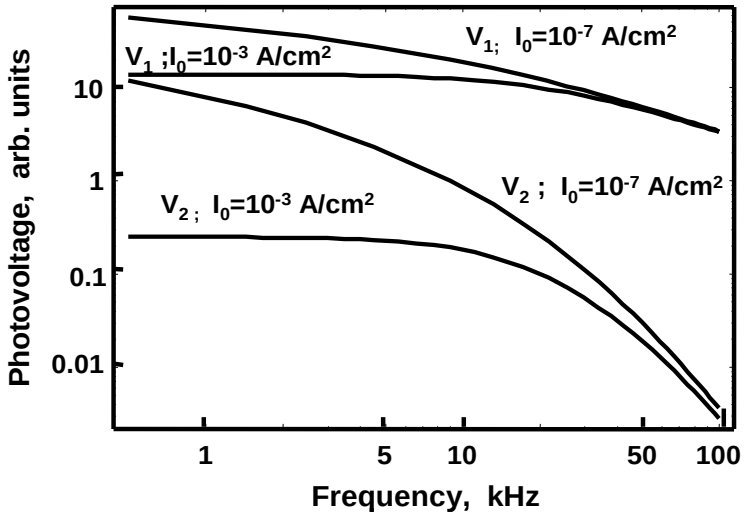

Figure 2. RsL and reverse-biased diode leakage current density versus peak trap density for USJs formed in halo profiles (N_D=2x10^{18}cm^{-3}).

By measuring the JPV at the two electrodes at different frequencies, combined with reference JPV measurements on a wafer with a deep p-n junction with known sheet resistance, the sheet resistance, R_s, conductance $G_{p\text{-}n}$ and capacitance of the p-n junction, $C_{p\text{-}n}$ can be simultaneously determined using measured voltages V_1 and V_2 and Eqs. (1) and (2). The measurement sequence is to first analyze V_1 and V_2 under high light modulation frequencies, where R_sx$C_{p\text{-}n}$, in Eq. 3 is the dominant term in the solution. This allows for a direct determination of the USJ sheet resistance, R_s, independent of junction depth or leakage current effects. The analysis is then repeated for a lower light modulation frequency, where $G_{p\text{-}n}$xR_s, is a more important factor. Since R_s is already determined at this point, $G_{p\text{-}n}$ (and J_{RsL}) can be determined directly.

Simulation Framework and Comparison with Experiment

A device simulation framework was developed to study the accuracy of RsL photovoltage analysis sketched in Eqs. 1 through 5 for ideal and non-standard profiles and measurement conditions. The main idea of the newly developed simulation framework is illustrated in the flowchart shown in Fig. 3.

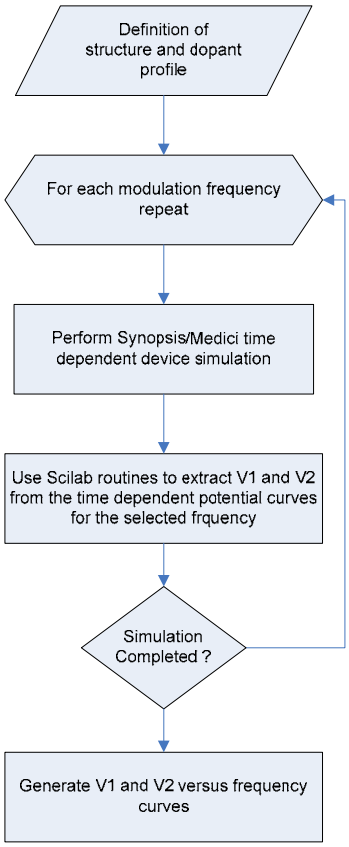

Figure 3. JPV simulation flowchart.

In this analysis, Synopsis/Medici device simulator input files are created which describe the mesh, the dopant profiles and the physical models to be used. These parameters contain a number of variables such as the modulation frequency of the light. The overall dataflow is controlled from within a series of Scilab [19] procedures. These procedures control a loop in which subsequently two main tasks are performed. First the time-dependent potential distributions at different lateral locations in a 2D axi-symmetric volume with appropriate size are calculated with Medici. Second, the integrated JPV signal under the two measurement probes V_1 and V_2 is extracted from the amplitude of the surface potential versus time curves. Finally, V_1 and V_2 are plotted versus modulation frequency, resulting in the so called frequency curves illustrated in Fig. 4. The final accuracy of these simulations depends critically on the physical models, the correct definition of the time dependent light beam source and the correct implementation of the underlying physics of the junction.

The main physical models used were Fermi-Dirac statistics, band gap narrowing, concentration dependent Philips mobility model and Shockley-Read-Hall (SRH) and Auger recombination. The experimental sinusoidal light beam variation was simulated as closely as possible with repetitive Gaussian shaped time dependence. Care must be taken when changing the modulation frequency that the integrated light intensity remains constant. Finally some defects need to be introduced near the junction in order to obtain realistic values for the junction leakage current (necessary to satisfy the underlying small signal assumption). Figure 4 illustrates the final result, which can be obtained when comparing the results from the simulations with the solutions from the analytical equations for the same structure. It shows that extremely good quantitative agreement can

be obtained. Furthermore, theory and simulations agree well with the experimental data (Fig. 4), for the simulation based on a perfect box profile approximation of the experimental SIMS dopant profile.

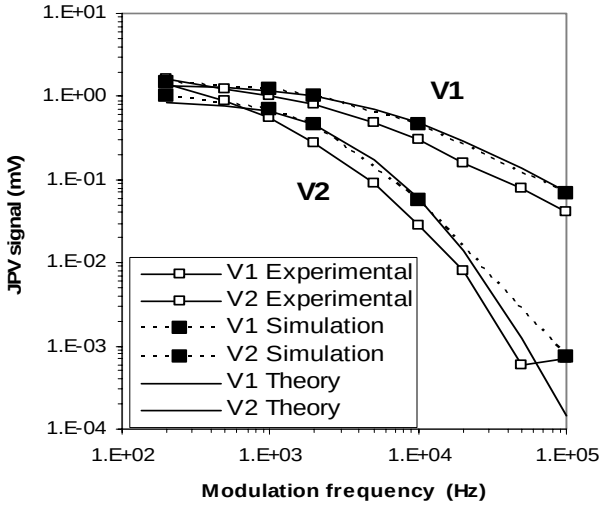

Figure 4. Simulated, theoretical and experimental frequency curves for V_1 and V_2. Simulation dopant structure was p-type box profile doped to $1.5x10^{19}/cm^3$ with thickness of 41 nm on top of medium doped n-type $7x10^{17}/cm^3$ layer. Light source was red light (650 nm) with an intensity of 10^{-4} W/cm^2.

Modeling Leakage Current

We compare the reverse-biased p-n junction leakage current measured by a contact probe technique with our contactless RsL technique. In our calculations we did not consider the additional reverse-biased diode thermionic emission currents from metal contacts to USJs. The p-n junction current density *J(V)* versus applied voltage *V* is determined by diffusion and recombination (generation) of excess carriers in the bulk, J_{diff}, through similar phenomena at the surface, J_S, through recombination (generation) with trap-assisted tunneling (TAT) in the depletion layer, J_{SCR}, and band-to-band tunneling current, J_{BTBT}

$$J(V) = J_{diff} + J_S + J_{SCR} + J_{BTB} = \left(q\frac{n_i^2}{N_D}\sqrt{\frac{D_n}{\tau_n}} + qs\frac{n_i^2}{N_A} \right)\left[e^{qV/kT} + 1\right] + J_{SCR}(V) + J_{BTBT}(V) \tag{6}$$

The recombination (generation) current $J_{SCR}(V)$ is obtained using [20, 21]

$$J_{SCR}(V) = q\int_{xj}^{xj+W} U(z,V)dz \tag{7}$$

where

$$U(z,V) \approx q(1+\Gamma)\frac{v_{th}\sigma_n\sigma_p N_t(z)(pn - n_i^2)}{\sigma_n(n+n_1) + \sigma_p(p+p_1)} \tag{8}$$

$$n = n_i \exp\left(\frac{q(\psi - \phi_n)}{kT}\right) \qquad p = n_i \exp\left(\frac{q(\phi_p - \psi)}{kT}\right) \tag{9}$$

$$n_1 = n_i \exp\left(\frac{E_t - E_i}{kT}\right); \qquad p_1 = n_i \exp\left(\frac{E_i - E_t}{kT}\right) \tag{10}$$

$$\Gamma = 2\sqrt{3\pi}\,\frac{E_r}{E_\Gamma}\exp\left(\frac{E_r}{E_\Gamma}\right) \;; \quad E_\Gamma = \frac{\sqrt{24m^*(kT)^3}}{q\hbar} \tag{11}$$

where N_A, N_D are the acceptor and donor concentrations in the top p-n junction layer and in the halo profile near the p-n junction, N_t, σ_n , σ_p are the trap concentration and electron and hole capture cross sections of recombination centers in the p-n junction depletion region, W the depletion region width, v_{th} the thermal velocity of carriers, n_i the intrinsic carrier concentration, s the surface recombination velocity, ψ the potential with respect to the semiconductor substrate, n_1 and p_1 the concentrations of electrons and holes when the Fermi level coincides with the trap level E_t, ϕ_n, ϕ_p the electron and hole quasi-Fermi levels, $V=\phi_n-\phi_p$, m^*(taken as $0.25m_0$) the effective mass, and E_r the localized electric field.

The band-to-band tunneling current density in the reverse-biased p-n junctions is

$$J_{BTBT}(V) = cqVE_m{}^{\sigma}\exp(-E_0/E_m) \tag{12}$$

where V is the applied junction voltage, E_m the maximum junction electric field and σ a numerical constant (σ=1 for direct tunneling and σ=3/2 for phonon-assisted tunneling) [22]. E_0 is a material constant which depends on the effective mass m^* and the semiconductor band gap. The prefactor c depends on the effective mass m^*, the band gap E_g and a factor describing electron-phonon interaction. In our calculations we used E_o=1.9x10^9 V/m, σ=3/2, c=1.6x10^{15}s^{-1} m$^{-1/2}$ V$^{-5/2}$ [22].

As shown in [6], in USJs the contribution of J_{diff} and J_S is small in comparison to recombination (generation) with trap-assisted tunneling in the depletion region, J_{SCR}, unless the dopants in p-type USJs are not activated and $N_A<<N_D$. For this reason we consider only trap-assisted tunneling and recombination-generation in the depletion region $J_{SCR}(V)$ and band-to-band tunneling current $J_{BTBT}(V)$. Also we consider non-degenerate n-type halos, where under forward bias, as in the case of RsL, band-to-band tunneling current is negligible [6].

The relevant equations for the diode leakage current density $J_D(V)$ for $V<0$ and RsL leakage current density J_{RsL} for $0<V<<V_T$ are

$$J_D(V) = J_{SCR}(V) + cqVE_m{}^{\sigma}\exp(-E_0/E_m) \tag{13}$$

$$J_{RsL} = \frac{kT}{q}\left.\frac{dJ_{SCR}(V)}{dV}\right|_{V\to+0} \tag{14}$$

The recombination profile $U(z, V)$ and leakage currents density $J_D(V)$ and J_{RsL} were calculated for an abrupt p-n junction, with junction depth x_j=10 nm, with a EOR residual damage profile described by

$$N_t(z) = N_{t\max}\exp\left(-\frac{q(z-z_{\max})^2}{\Delta^2}\right) + N_{tsub} \tag{15}$$

where N_{tmax} is the peak recombination centers concentration at a depth of z_{max}=20 nm, with a trap profile width of Δ=15 nm, $\sigma_n = \sigma_p = 10^{-14}$ cm^2, $E_t = E_i$ and $N_{tsub} = 10^{12}$ cm^{-3} is the trap concentration in the substrate, much deeper than z_{max}. These parameters approximate the conditions for shallow junctions formed in implanted halo profiles. For modeling of leakage current for CVD-grown USJs we considered traps to be localized in the interface between the USJ layer and the medium-doped epi-layer with $z_{max} = x_j$=10 nm , Δ=1 nm.

The recombination (generation) rate *U(z,V)* profiles for substrate and halo doping concentrations of $N_D = 10^{15}$ cm^{-3} and $N_D = 10^{18}$ cm^{-3} are shown in Fig. 5. With increasing reverse bias the width and magnitude of the recombination rate profiles increase and the leakage current increases. In the case of low doping concentration $N_D = 10^{15}$ cm^{-3}, typical of 10 ohm-cm resistivity Si test wafers, the recombination rate profile does not overlap the residual damage profile $N_t(z)$ and hence the leakage current is low (Fig. 6). With increasing halo doping concentration, the depletion region width decreases and the recombination profile overlaps the implant residual damage profile (Fig. 5) causing the leakage current to rise by a few orders of magnitude, as shown in Fig. 6. In the case of CVD-grown USJs, traps are mainly localized at the interface (x_j) and the leakage current is low in the doping concentration range $N_D < 10^{18}$ cm^{-3} where TAT and BTBT are not significant. Trap-assisted and band-to-band tunneling for $N_D > 10^{18}$ cm^{-3} increase the leakage current further when the depletion region width is *W*~10 nm. In the case of CVD USJs, the BTBT leakage is the main contributor for $N_D > 10^{18}$ cm^{-3}.

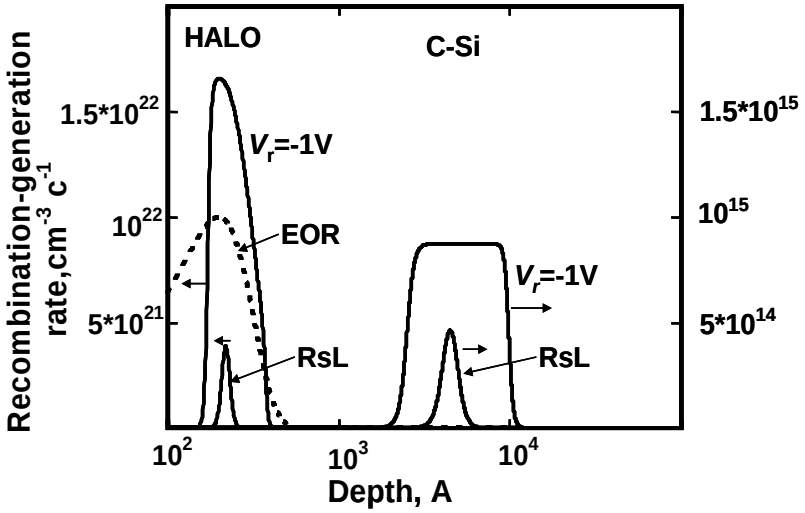

Figure. 5 Carrier recombination-generation rates *U*(*z*,*V*) versus depth for USJ with x_j=10 nm formed in a standard c-Si substrate $N_D = 10^{15}$cm^{-3} and halo $N_D = 10^{18}$cm^{-3} for RsL and reverse-biased diode with *Vr*=-1V; dashed line shows the residual EOR damage profile $N_t(z)$.

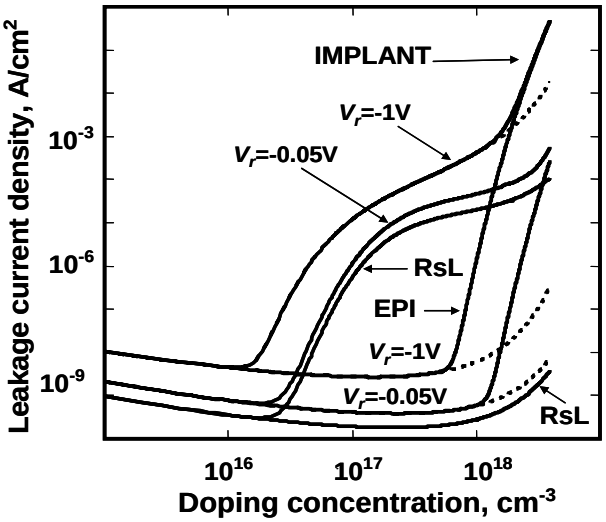

Figure 6. RsL and reverse-biased diode leakage current versus substrate doping concentration for implant (N_{tmax}=10^{17}cm^{-3}) and CVD EPI (N_{tmax}=10^{21}cm^{-3}) USJs. Dashed curves show the leakage current without BTBT contribution.

Figure 7 shows the RsL J_{RsL} and reverse-biased leakage current densities $J_D(V)$ for V_r=-1V, -0.5 V and V_r=-0.05V of USJs formed in a halo profile with N_D=2x10^{18} cm^{-3} are shown as a functions of trap density. For high reverse bias, the leakage current $J_D(V)$ is significantly higher than J_{RsL} especially for low trap densities where the contribution of BTBT is significant. With decreasing bias ($|Vr|$<0.05V) J_{RsL} and $J_D(V)$ are similar. The same results were obtained in [8] using numerical simulation.

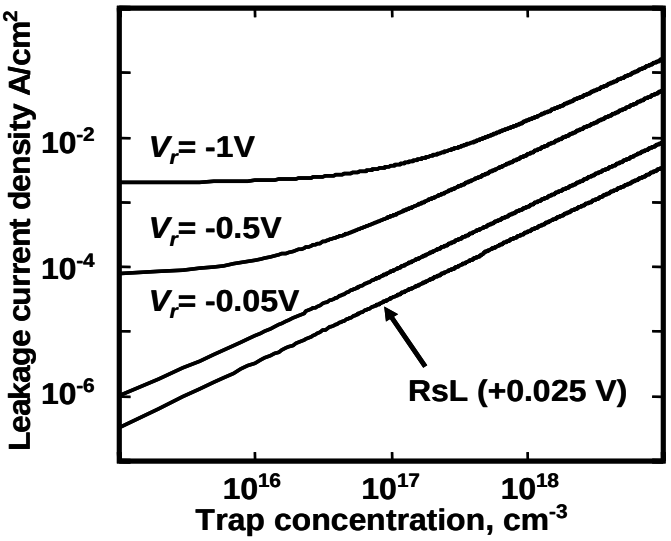

Figure 7. RsL and reverse-biased diode leakage current density versus peak trap density for USJs formed into halo profiles (N_D=2x10^{18}cm^{-3}).

Effect of the Halo on Sheet Resistance and Leakage Current

We will use the above theory to explain experimental RsL leakage data [12,13] from USJs formed with low energy implant and spike, millisecond anneal and low temperature CVD grown boron-doped USJs. In [12.13] millisecond anneals were performed using flash system (fRTP), where the wafer is rapidly heated to an intermediate temperature and its front surface is then heated further by a <1.5 ms pulse from a bank of flash-lamps [10]. The wafers were (100) oriented, n-type with ρ>2 ohm-cm. The study included comparisons of 10^{15} B/cm^2 at 500 eV and 5 keV Boron implants into crystalline (c-Si) and implant-amorphized (PAI) silicon, the effects of halo doping concentration and the impact of annealing the halo implant before implanting the USJ. The pre-amorphization implants (PAI) were 10^{15} Ge/cm^2 at 30 keV and the halo implants were $4x10^{13}$ As/cm^2 at 40 keV. In some samples the halo implants were annealed for 10 s at 1050°C before the PAI or B implants. The final anneals were either a spike anneal at 1050°C or fRTP with a preheating to intermediate temperature T_i followed by a jump to temperature T_p. Low-temperature CVD boron-doped USJ layers were grown with a doping concentration of about $2x10^{19}$ cm^{-3} on a 20 μm thick medium arsenic-doped ($7x10^{17}$ cm^{-3}) epi-layer grown on ~10 ohm-cm n-Si substrate. USJ thickness ranged from 132 nm down two 2 nm [9].

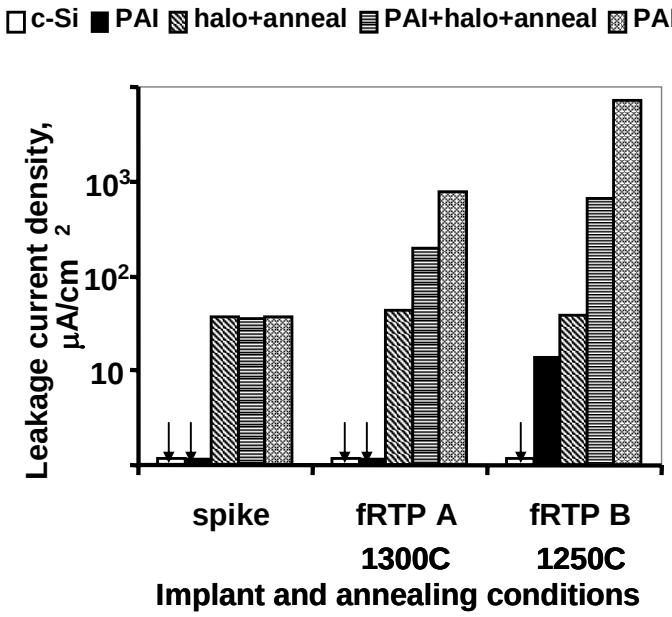

Figure 8. Leakage current density for junctions formed by 500 eV B implants into various samples, annealed by various methods [12].

Fig. 8 shows the junction leakage current density trends for several conditions. Spike anneals give consistently low leakage current, regardless of the implant scheme, most likely because dopant diffusion during the spike anneals can drive the junction deeper than the residual implant damage. As result, the recombination profiles located in the middle of the depletion region do not overlap with the residual implant damage distribution and leakage current is low. Furthermore, for sufficiently high peak temperatures, spike annealing can effectively eliminate residual damage [23]. In agreement with Fig. 6. the leakage current density for implants without halo ("c-Si", "PAI") doping was below the measurement limit of 0.1 μA/cm^2, except for the case of

fRTP at 1250ºC with Ge PAI damage. In agreement with Fig. 6 the presence of halo doping consistently increases the leakage current because of the greatly reduced depletion layer width and the overlap of the peak recombination rates with the residual implant damage distribution as shown at Fig.5. Annealing the halo implant damage prior to the B ("halo+anneal") doping steps significantly improved the leakage current. Ge PAI damage resulted in significant leakage current after fRTP anneals at 1250°C, but 1300°C anneals were more effective in reducing leakage currents.

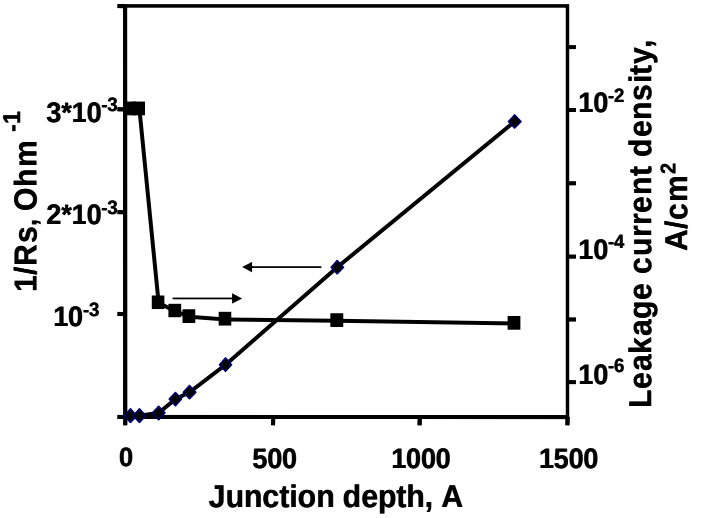

Figure 9. Inverse sheet resistance and leakage current density versus layer thickness for USJs formed by CVD growth of a highly-doped p-Si layer.

Fig. 9 shows the RsL inverse sheet resistance and junction leakage current versus junction thickness for CVD-grown USJs. Significant increase of leakage current and sheet resistance exceeding the high limits of RsL ($>10^{-2}$ A/cm^2, $>10^5$ Ohm/sq) is observed only for USJs with x_j=1.7 nm and x_j=4.8 nm. In agreement with *C-V* data, these USJs do not have active p-n junctions [9]. The intercept of the $1/R_s$ trend at ~8 nm indicates that the CVD growth process resulted in an inactive dopant layer of ~8 nm for all layers, corresponding to the high R_s ($>10^5$ ohm/square) and high leakage current seen for $x_j < 10$ nm, shown in Fig. 5 [9]. For CVD layers thinner than 10 nm, the lack of p-n junction activity, seen in the RsL measurements as the lack of strong JPV signals and high R_s and leakage currents, could be due to either structural defects incorporated during the initial stage of the growth process or depletion effects from charged states at the growth interface, or from a combination of these effects. CVD-grown USJs with x_j>100A show low leakage current (see Fig.9), since a recombination profile located in the middle of depletion layer does not overlap with the recombination centers located mainly at the growth interface.

Conclusion

We have presented the relevant theory, confirmed by experimental data, of the sheet resistance and leakage current (RsL) method for ultra-shallow junction (USJ) characterization and have shown that the underlying junction photo-voltage (JPV) theory is well understood, and that accurate Medici-based device simulations are available to investigate the JPV behavior for non-ideal cases. This study furthermore demonstrates the importance of characterizing USJ formed in halo profiles for 65 and 45 nm ULSI. The

results reveal the challenges remaining for incorporation of ms-timescale anneals for CMOS fabrication and highlight the importance of basing process choices on accurate quantitative information of dopant activation and leakage currents for highly-doped, multi-profile junctions. Reverse-biased diode and non-contact RsL leakage currents are similar for low reverse bias $V < kT/q$. For higher reverse bias (V>>kT/q) leakage currents are generally higher than those reported by RsL leakage measurements as a result of contributions from band-to-band tunneling and increased trap-assisted tunneling. Significantly higher leakage currents are observed for USJ formed in highly-doped halo profiles due to high carrier recombination-generation rates increased by trap-assisted tunneling and band-to-band tunneling. The levels of leakage current depend on many process factors, including dopant profiles and activation as well as the location and density of residual damage after annealing, together with measurement conditions such as the sign and magnitude of junction bias.

The opportunities for process optimization can be seen in the systematic improvements in leakage currents that are observed with RsL measurements for USJ formed in halo profiles where the As implant damage has been reduced by annealing prior to the B doping steps. Optimization of USJ formation using advanced annealing requires careful balance of halo "strength" and shallow junction doping, balancing control of short-channel effects with leakage currents. Accurate process monitoring of USJ formed with ms-timescale anneals requires the inclusion of a comprehensive set of interacting implant profiles and thermal processing (halo, PAI, SDE and anneals) in order to provide reliable guidance for process decisions. The challenges posed by the thin (~10 nm) dopant layers and high leakage current densities ($>10^{-4}$ A/cm^2), which are characteristic of these combined profiles, rule out the use of contact probes, such as conventional four-point probes, and favor the use of non-contact measurements of sheet resistance and leakage current, provided by RsL methods.

Acknowledgements

We acknowledge A. Koo for support of this project and P. Timans, A. Moussa, T. Zangerle, F. Schaus, and J. Halim for many contributions.

References

1. R.S. Nakhamson, *Solid State Electron*., **18**, 617-626 (1975).
2. J.E. Park, D.K. Schroder, S.E. Tan, B.D. Choi, M. Fletcher, A. Buczkowski, and F. Kirscht, *J. Electrochem. Soc*., **148**, G411-G419 (2001).
3. Gerald Lucovsky*, J. Appl. Phys*. **31**, 1088(1960).
4. V. Faifer, V. Dyukov, A. Pradivtsev, D. Skurida, Proc. 24th European Solid State Device Research Conf. (ESSDERC'94) I.O.P. 601-604 (1994).
5. US Patent 5,442,297 Verkuil, Roger L, (1995).
6. V.N.Faifer, D.K. Schroder, and M.I.Current, *Appl.Phys. Let.,*89,151123 (2006).
7. V.N. Faifer, M.I. Current, T.M.H. Wong, and V.V. Souchkov, *J. Vac. Sci. Technol*. **B24**, 414-420 (2006).
8. T. Clarysse, A. Moussa, T. Zangerle, F. Schaus, W. Vandervorst, V.N. Faifer, and M.I. Current, Proceedings INSIGHT-2007 Workshop (May, 2007, Napa, CA, submitted to JVST B).
9. T. Clarysse, A. Moussa, F. Leys, R. Loo, W. Vandervorst, M. C. Benjamin, R. J. Hillard, V. N. Faifer, M. I. Current, R. Lin, and D.H. Petersen, *Mat. Res. Soc. Symp. Proc*., **912**, 0912-C05-07, 2006.
10. P. Timans, J. Gelpey, S. McCoy, W. Lerch, and S. Paul, *Mat. Res. Soc. Symp. Proc*., **912**, 0912-C01-01, 2006.

11. V.N. Faifer, D.K.Schroder, M.I.Current, T.Clarysse, P.J. Timans, T. Zangerle, W. Vandervorst, T.M.H.Wong, A.Moussa, S. McCoy, J. Gelpey, W. Lerch, S. Paul, D. Bolze, Proc. Frontiers of Characterization and Metrology for Nanoelectronics (March, 2007, Gaithersburg, MD, to be published by A.I.P. 2007).
12. V.N. Faifer, D.K.Schroder, M.I.Current, T.Clarysse, P.J. Timans, T. Zangerle, W. Vandervorst, T.M.H.Wong, A.Moussa, S. McCoy, J. Gelpey, W. Lerch, S. Paul, D. Bolze, Proceedings INSIGHT-2007 Workshop (May, 2007, Napa, CA, submitted to JVST B).
13. V.N. Faifer, D.K.Schroder, M.I. Current, T. Clarysse, P.J. Timans, T. Zangerle, W. Vandervorst, T.M.H.Wong, A. Moussa, S. McCoy, J. Gelpey, W. Lerch, S. Paul, D. Bolze, To be published in JVSTA.
14. M. Manssori, A. Jain, D. E. Mercer, L. Robertson and P. Kohli, *Electrochem. Soc. Proc.* **2000-11**, p.389-412 (2002).
15. R. Lindsay, K. Henson, W. Vandervorst, K. Maex, B. J. Pawlak, R. Duffy, R. Surdeanu, P. Stolk, J. A. Kittl, S. Giangrandi, X. Pages, and K. van der Jeugd , *J. Vac. Sci. Technol.* **B22**, 306-311 (2004).
16. P. M. Solomon, D.J. Frank, J. Jopling, C. D'Emic, O. Dokumaci, P. Ronsheim, and W.E. Haensch, *IEEE IEDM*, 9.3.1-9.3.4 (2003).
17. J.E. Park, J. Shields, and D.K. Schroder, *Solid-State Electron*., **47**, 855-864 (2003).
18. E.C. Jones and N.W. Cheung, *J. Vac. Sci. Technol*. **B14**, 236-241 (1996).
19. Scilab open source platform for numerical calculation (www.scilab.org).
20. S.M. Sze, *Physics of Semiconductor Devices*, 2nd ed. (Willey, New York, 1981).
21. G.A.M. Hurkx, D.B.M. Klassen, and M.P. Knuvers, *IEEE Trans. Electron Dev*. **39**, 2090-2098 (1992).
22. G.A.M. Hurkx, *Solid-State Electron*., **32**, 665-668 (1989).
23. W. Lerch, S. Paul, J. Niess, S. McCoy, T. Selinger, J. Gelpey, F. Cristiano, F. Severac, M. Gavelle, S. Boninelli, P. Pichler , and D. Bolze, *Mat. Sci. and Eng*. B., **124–125**, 24 (2005).